Title

Visualizing electron localization of WS2/WSe2 moiré superlattices in momentum space

Journal

Science Advances, 7(37)

ISSN

2375-2548

Authors

Stansbury, Conrad H
Utama, M Iqbal Bakti
Fatuzzo, Claudia G
et al.

Publication Date

2021-09-10

DOI

10.1126/sciadv.abf4387

Peer reviewed

CONDENSED MATTER PHYSICS

Visualizing electron localization of WS_2/WSe_2 moiré superlattices in momentum space

Conrad H. Stansbury[1,2]*, M. Iqbal Bakti Utama[1,2,3], Claudia G. Fatuzzo[2†], Emma C. Regan[1,2,4], Danqing Wang[1,2,4], Ziyu Xiang[1], Mingchao Ding[1], Kenji Watanabe[5], Takashi Taniguchi[6], Mark Blei[7], Yuxia Shen[7], Stéphane Lorcy[8], Aaron Bostwick[9], Chris Jozwiak[9], Roland Koch[9], Sefaattin Tongay[7], José Avila[8], Eli Rotenberg[9], Feng Wang[1,2,10], Alessandra Lanzara[1,2,10]*

The search for materials with flat electronic bands continues due to their potential to drive strong correlation and symmetry breaking orders. Electronic moirés formed in van der Waals heterostructures have proved to be an ideal platform. However, there is no holistic experimental picture for how superlattices modify electronic structure. By combining spatially resolved angle-resolved photoemission spectroscopy with optical spectroscopy, we report the first direct evidence of how strongly correlated phases evolve from a weakly interacting regime in a transition metal dichalcogenide superlattice. By comparing short and long wave vector moirés, we find that the electronic structure evolves into a highly localized regime with increasingly flat bands and renormalized effective mass. The flattening is accompanied by the opening of a large gap in the spectral function and splitting of the exciton peaks. These results advance our understanding of emerging phases in moiré superlattices and point to the importance of interlayer physics.

INTRODUCTION

In a stack of two-dimensional (2D) materials, the formation of a moiré superlattice provides a method for engineering electron behavior at a controlled momentum and energy scale via the modified electrostatic and strain environments. Superlattices can originate either due to a lattice constant mismatch δ between the interface layers or due to their rotational misalignment θ, where the periodicity λ is given by

$$\lambda = \frac{(1+\delta)a}{\sqrt{2(1+\delta)(1-\cos\theta)+\delta^2}}$$

In the single-particle picture, superlattices can markedly modify the electronic states at low energy via zone folding. The periodic variation in lattice alignment introduces an associated mini-Brillouin zone with corresponding mini-bands and enhancement of the effective mass. Further, lattice reconstruction becomes energetically favorable when the superlattice periodicity becomes sufficiently large, driving further modification to the electronic states.

These effects provide an opportunity to engineer the entire band structure toward a functional purpose or toward the realization of exotic phases. Under appropriate conditions, the on-site potential can even dominate the mini-bandwidth and drive correlated phases to emerge on the superlattice (*1*–*8*). In superlattices formed by semiconducting transition metal dichalcogenides (TMDCs), modifications to the excitonic sates have also been observed (*9*–*11*).

Direct measurements of the superlattice electronic band structure may provide important insights into the emergence of the correlated phases. In particular, angle-resolved photoemission spectroscopy (ARPES) is an ideal and direct tool to measure electronic band structure and many-body effects. However, ARPES measurements on 2D heterostructures are challenging due to stringent sample and experimental requirements, including a small beam diameter (<10 μm) to probe small samples and an exposed sample surface. To overcome these limitations, most prior studies used large, but lower-quality chemical vapor deposition–grown films (*12*, *13*) or samples without control of interlayer alignment (*14*). Further, no ARPES studies exist on TMDC heterostructures that simultaneously display moiré excitons or other hallmarks of strong superlattice modification. As a result, the consequences of strong band structure modifications in large wavelength TMDC superlattices remain essentially unexplored by the most direct technique.

Here, we report the first such study in WS_2/WSe_2 TMDC superlattices through combined optical absorption spectroscopy and nano-ARPES with beam diameter smaller than 2 μm. Whereas heterostructures with large twist angles—and corresponding small superlattice wave vectors—reproduce the spectral functions of the constituent monolayers, nearly aligned superlattices of WS_2/WSe_2 exhibit marked modification of the electronic bands. In these samples, we observe renormalization of the binding energies of the low-energy W *d*-bands [at both the zone edge (*K*) and the zone center (Γ)], an opening of a bonding-antibonding–like splitting at the Γ point at a large energy scale, and a splitting of the exciton peaks by the superlattice potential in agreement with previous reports (*9*–*11*). Most directly, these features also accompany marked flattening of the low-energy bands at Γ, a sign of localization of valence electrons even away from the band edge at the *K* point.

[1]Department of Physics, University of California Berkeley, Berkeley, CA 94720, USA. [2]Materials Sciences Division, Lawrence Berkeley National Laboratory, Berkeley, CA 94720, USA. [3]Department of Materials Science and Engineering, University of California Berkeley, Berkeley, CA 94720, USA. [4]Graduate Group in Applied Science and Technology, University of California Berkeley, Berkeley, CA 94720, USA. [5]Research Center for Functional Materials, National Institute for Materials Science, 1-1 Namiki, Tsukuba 305-0044, Japan. [6]International Center for Materials Nanoarchitectonics, National Institute for Materials Science, 1-1 Namiki, Tsukuba 305-0044, Japan. [7]School of Engineering of Matter, Transport and Energy, Arizona State University, Tempe, AZ 85287, USA. [8]Synchrotron-SOLEIL and Université Paris-Saclay Saint-Aubin, BP48, F91192 Gif sur Yvette Cedex, France. [9]Advanced Light Source, Lawrence Berkeley National Laboratory, Berkeley, CA 94720, USA. [10]Kavli Energy NanoSciences Institute at the University of California Berkeley and the Lawrence Berkeley National Laboratory, Berkeley, CA 94720, USA.
*Corresponding author. Email: chstansbury@lbl.gov (C.H.S.); alanzara@lbl.gov (A.L.)
†Present address: Istituto di Scienze del Patrimonio Culturale, Consiglio Nazionale delle Ricerche (ISPC-CNR), Via Biblioteca 4, 95124 Catania, Italy.

RESULTS

WS_2 and WSe_2 superlattices were prepared on SiO_2 substrates with an intermediate layer of graphite or hBN, as schematically shown in Fig. 1A, to enable optical and photoemission spectroscopy measurements on the same sample. As ARPES requires access to the sample surface, samples were prepared either with a monolayer graphene cap or via polypropylene carbonate (PPC) transfer with inversion to leave a clean vacuum-exposed superlattice (see Materials and Methods). To explore the evolution of the electronic structure in the presence of superlattices of varying wavelength, we fabricated heterostructures with a different relative alignment between the two TMDC monolayers. We focus principally on two heterostructures, a sample with a small misalignment (<1°), giving rise to a large superlattice vector of λ = 7 nm and another with a larger misalignment (6°) and smaller superlattice vector λ = 2.8 nm. Figure 1B shows a schematic of sample S1 in momentum space, including the Brillouin zones for the monolayers and the superlattice Brillouin zone (dark gray).

Because both heterostructures have an area of <200 μm^2, we used a beam size of less than 2 μm to allow separate photoemission measurements of the monolayers and of the heterostructure (see Materials and Methods). Figure 1C shows an optical microscope image of the λ = 7.0 nm sample, where the yellow and purple regions are WSe_2 and WS_2, respectively, and the heterostructure is the yellow/purple overlapped region. Because the tungsten 4f core levels have different binding energies in WS_2 and WSe_2, the identification of monolayer and heterostructure regions is corroborated by spatially resolved photoemission spectra at the tungsten 4f level. These results are shown in Fig. 1D, where the core-level peak energy is plotted across the sample. Because of the surface sensitivity of ARPES, when measuring the heterostructure region most of the photoemission yield comes from the vacuum-exposed layer. Despite weaker intensity for the buried layer, a small complementary shift of <50 meV is observed for the core levels of WS_2 and WSe_2.

Figure 1E shows the valence band spectra for the individual TMDC monolayers (left) and the two superlattices (center and right) at the zone center (Γ) and zone boundary (*K*). The λ = 7 nm sample shows the most marked spectral differences (right curves, Fig. 1E): The energy splitting between the two lowest energy peaks is increased by 300 meV, indicating a strong modification of the valence density of states in this superlattice. Furthermore, the line shapes are asymmetric, in contrast to the symmetric peaks that are usually observed in the spectral function and which we observe in monolayer samples (Supplementary Materials). On the other hand, the valence band for the λ = 2.8 nm sample (central curves, Fig. 1E) is consistent with a weighted combination of the valence bands of each individual layer.

Using nano-ARPES, we measured the electronic structure for the monolayers (Fig. 2, A and B) and for the two superlattices with small and large superlattice vectors (Fig. 2, C and D), along the Γ*K* high symmetry direction (Fig. 2F). In agreement with previous ARPES studies (*15*–*17*), theoretical models (*18*–*21*), and the tight-binding calculations shown in Fig. 2E, locally parabolic bands at Γ disperse with a clearly resolved spin-orbit splitting to the *K*/*K*′ high symmetry. The excellent correspondence to theory and the narrow linewidths demonstrate the high quality of the studied samples.

For the sample with the smaller superlattice vector (λ = 2.8nm), the ARPES spectrum is largely a superposition of the individual monolayer spectra. Both spectra, however, have undergone a rigid

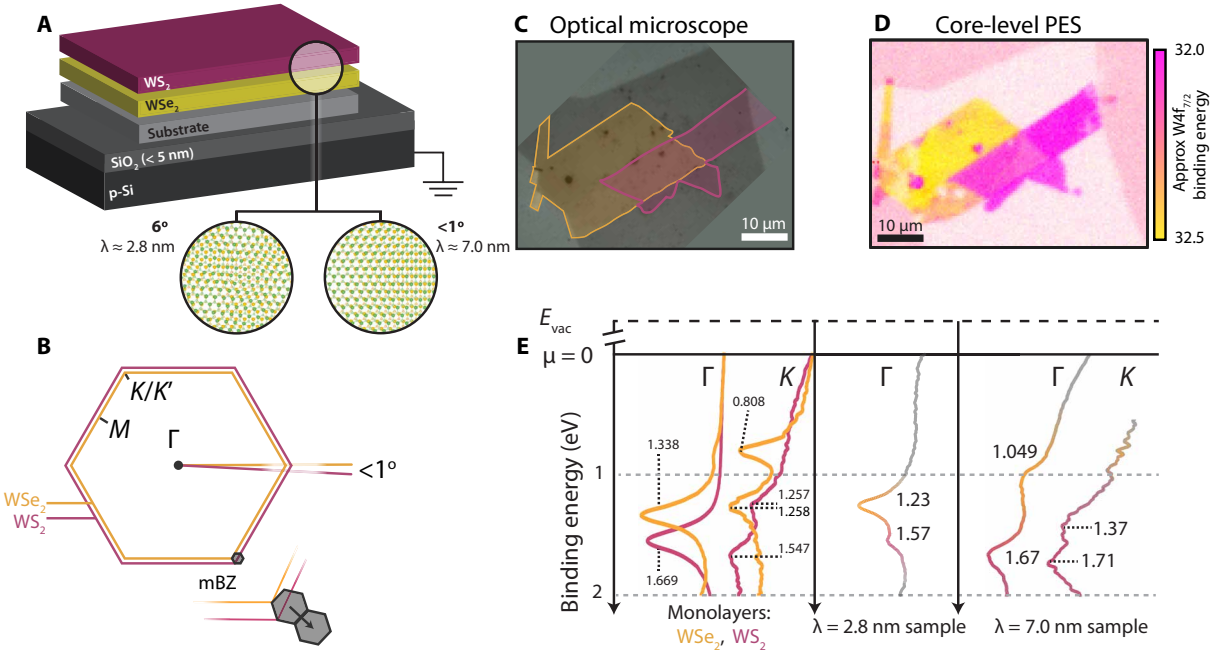

Fig. 1. Micro-ARPES of exfoliated TMDC heterostructures. (**A**) Sample geometry for the photoemission and optical experiments. (**B**) Brillouin zone for sample S2 (1°). The 4.4% lattice mismatch between WS_2 (0.318 nm) and WSe_2 (0.332 nm) creates a mini-Brillouin zone (mBZ) (dark gray) at the WS_2/WSe_2 zone corner. (**C** and **D**) Optical and photoemission maps of sample S1. In the optical image, the WSe_2 monolayer is highlighted in yellow, and the WS_2 monolayer is in purple. In the core-level maps, the intensity corresponds to the ratio of weight in a 100-meV window around the monolayer 4f core levels for WS_2 (purple) and WSe_2 (yellow). (**E**) Energies of the essential band structure features in monolayers (left) and heterostructures (middle, right) demonstrating substantial changes to the valence band spectrum in the 7.0-nm sample (right) but not in the 2.8-nm sample (middle).

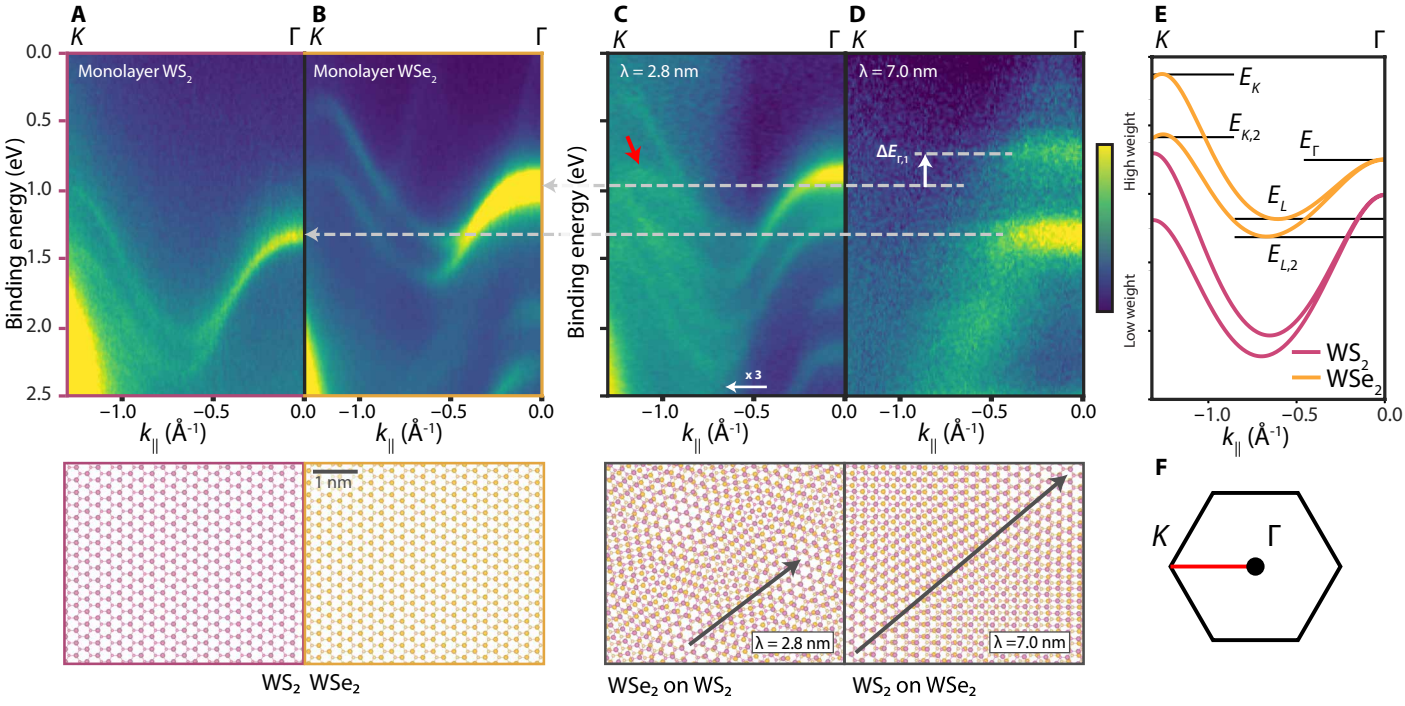

Fig. 2. High-symmetry band structure. (**A** to **D**) Measured high-symmetry dispersions for WS_2 monolayer (A), WSe_2 monolayer (B) collected from nonoverlapping portions of the λ = 2.8 nm sample (C), and aligned heterostructure (D). Below each ARPES spectrum is the lattice structure for each system. ARPES spectra recorded from the λ = 2.8 nm sample show only a small rigid band shift compared to the monolayer spectrum, while in aligned samples the WSe_2 originating band is substantially shifted toward smaller binding energy and both bands are renormalized to larger effective mass. Additional dispersing bands observable near the *K* point in (C) are due to the presence of a small piece of WSe_2 monolayer on graphite (relative alignment, 5°, red arrow), also under the beam. For monolayers and the misaligned heterostructures, beam sizes smaller than 10 μm were used, while beams smaller than 1.5 μm were used for all presented data of λ = 7 nm samples. Dashed lines across (A) to (D) show the valence band edge, with the change in energy between the band edges in the λ = 7.0 nm sample annotated as $\Delta E_{\Gamma,1}$. (**E**) Tight-binding calculation of the valence band structure for individual monolayers. Energy degenerate bands at the Γ point evolve continuously to spin-orbit split bands at the *K*/*K*′ points where there is a direct bandgap. (**F**) Momentum direction for the data presented in (A) to (D) in the monolayer WS_2 Brillouin zone.

shift toward the chemical potential by less than 100 meV, consistent with the increased dielectric screening relative to monolayers on graphite (*22*). By contrast, in the sample with the larger superlattice vector, λ = 7.0 nm, the electronic structure is markedly modified relative to the monolayers (Fig. 2E). We observe three main features: (i) a visually apparent flattening of the bands at Γ, (ii) an increased binding energy offset (in Fig. 2E, annotated as $\Delta E_{\Gamma,1}$) between the two lowest energy bands (Fig. 2, B to E, dashed lines) at Γ, and (iii) an increase and asymmetry of the spectral linewidth across the observed momentum region. These three features are observed in each of two aligned samples we studied by nano-ARPES (see the Supplementary Materials). Before unpacking this phenomenology, we turn to take a more granular look at the ways in which the band structure is renormalized.

Figure 3 shows a closer look of the energy renormalization effects at the Γ and *K* points in the two heterostructures along selected momentum directions mapped in Fig. 3I. In addition to the energy shift discussed above, a strong flattening of the bands is observed near the zone center for the λ = 7.0 nm heterostructure (Fig. 3A), but not in the λ = 2.8 nm heterostructure (Fig. 3B). This flattening is even clearer from the comparison of the energy distribution curves (EDCs), or spectra at constant momentum, shown in Fig. 3 (C and D). The momentum location of the spectra is indicated by the vertical tick marks in the *x* axis of Fig. 3 (A and B). For the smaller λ = 2.8 nm superlattice sample, two sharp well-separated and dispersing peaks are observed, corresponding to the modified valence bands from the WSe_2 and WS_2 layers (Fig. 3D). When plotting the peak position as a function of momentum (purple and yellow dots overlayed in the raw image plot in Fig. 3B), we can follow the valence band dispersion of each monolayer all the way down to the valence band minimum in sample S2. In contrast, for the λ = 7.0 nm sample, three weakly dispersive peaks are observed (Fig. 3C), which give rise to highly localized (nondispersive) bands as shown in Fig. 3A. If we directly compare the dispersions in 3c and 3d, the WS_2 monolayer valence band (purple peak series, Fig. 3D) is gapped by 450 meV along the band to correspond to two distinct peak series (dark gray peaks 3c, curves 2 to 9) in the λ = 7.0 nm sample.

Figure 3 (E and F) shows ARPES spectra across the *K* point in the λ = 7 nm and λ = 2.8 nm heterostructures. As near the zone center (Fig. 3, A and B), we observe a flattening of the band structure for the λ = 7 nm sample (Fig. 3E) for each of the spin-orbit split branches at the *K* point. However, at the *K* point, the spectra are overall more diffuse than at the zone center, as is expected due to mini-band formation with the larger native effective mass (≈0.4m_0) and the lower overall photoemission yield from K in WS_2 and WSe_2. We extract the dispersion from the local maximum of the intensity, which is plotted as red circles over the image plots in Fig. 3 (E and F). A comparison between extracted dispersion for the two samples and a monolayer tight-binding model for WS_2 is shown in Fig. 3G. We find excellent correspondence between the weakly coupled λ = 2.8 nm

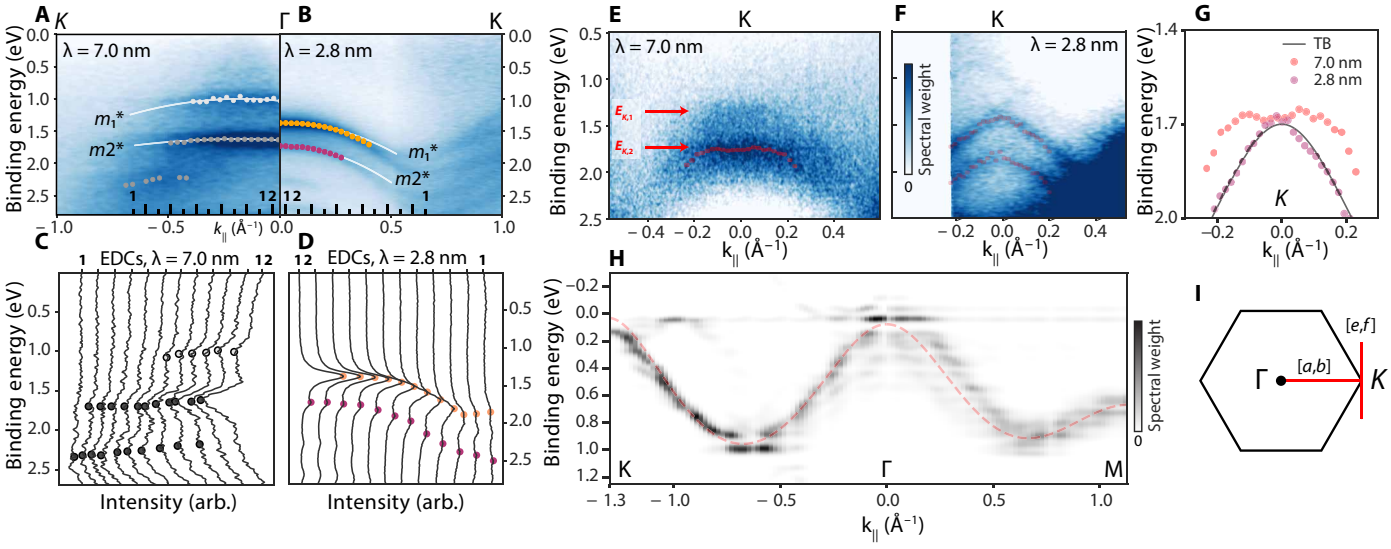

Fig. 3. Renormalized band structure of long-wavelength TMDC superlattices. (**A** and **B**) Dispersions along Γ*K* for the λ = 7.0 nm (A) and λ = 2.8 nm sample (B). Flattening of the bands is observed for the λ = 7.0 nm heterostructure. Dots indicate peak locations from EDC fitting. White lines indicate fits for quadratic bands within 0.2 Å^{-1} of Γ. (**C** and **D**) Energy distribution curves taken along the indicated cuts at the bottom of (A) and (B). The λ = 2.8 nm sample (D) shows sharp, continuously dispersing peaks, while the bands in the λ = 7.0 nm sample (C) are nondispersive to the band bottom near EDC 1. In (C) and (D), dots indicate intensity maxima. (**E** and **F**) Spectra taken at *K* perpendicular to the Γ*K* direction for the 7.0 nm (E) and 2.8 nm (F) samples. The 7.0 nm sample shows nondispersing features. Red circles show peak positions from EDC fitting for the larger binding energy band (both bands) in the 7.0 nm (2.8 nm) sample. In (E) and (F), an affine background was subtracted. (**G**) Comparison of the absolute energies of recovered peaks for WS_2 tight binding (TB), 2.8 nm, and 7.0 nm dispersions shown in (E) and (F). From the dispersion in the λ = 7.0 nm sample, we estimate the width of *K* point as ~3 nm^{-1}. (**H**) Spectral function for a three-band TB model of WS_2 with a superlattice periodic on-site energy, reproducing flattening at the valence band edge. The dashed red curve traces the bare valence band dispersion. (**I**) Momentum direction for (A), (B), (E), and (F) in the monolayer Brillouin zone.

sample and the monolayer tight binding. By contrast, notable flattening at the *K* point is observed in the λ = 7.0 nm heterostructure, including a possible concavity consistent with mini-band formation at *K* (Supplementary Materials). From the flattened region around the lower *K*-point band edge, we determine that the width of the low-energy state whose dispersion is traced in Fig. 3G is between 3 and 4 nm^{-1}. From ARPES on twisted bilayer graphene moirés (*23*, *24*), dimensional crossover in nanowires (*25*), and from ARPES on aromatic hydrocarbons (*26*), width photoemission features in localized systems are related inversely to spatial confinement of the system. From the measured width in momentum, we can estimate the localization of electrons in the supercell with local density of states contributing to the *K*-point band edge by calculating via the uncertainty principle $\Delta\lambda\Delta k = 2\pi$ to be 1.6 to 2.1 nm. Because the supercell λ exceeds 7 nm, our observations verify that the lowest energy electrons at the band edge are highly localized around a few lowest energy patches in the superlattice. The recovered values for the localization of the band edge states are in extremely good correspondence with the value of around 2 nm found by scanning tunneling spectroscopy (STS) for the WSe_2 valence mini-band in WS_2/WSe_2 (*27*). Details concerning applicability of the uncertainty principle and the connection between spectral function broadening and the confinement of the localized states can be found in the Supplementary Materials.

We constructed a three-band tight-binding model of WS_2 with a superlattice periodic on-site perturbation due to the presence of the WSe_2 layer (the detailed procedure is available in the Supplementary Materials). This model permits an examination of which of the observed spectral features can be assigned to structural effects, which are modeled effectively without recourse to the partner layer in the heterostructure through modifications to the on-site and hopping terms. The bands were unfolded to produce the spectral function on the first Brillouin zone of WS_2 and are shown along the high symmetry directions in Fig. 3H. Upon the introduction of only a moderate on-site perturbation of 100 meV or with a comparable perturbation to the hopping terms, our model reproduces essentially flat bands at the top and bottom of the valence band, in agreement with our ARPES results and over a comparably large momentum range. The on-site perturbation of 100 meV was chosen conservatively smaller than the linewidth broadening to demonstrate that localization can occur even with a moderate perturbation. The degree of flattening at each of the Γ and *K* points can be independently tuned by the degree of modulation of the on-site energy for the relevant orbitals. While this model captures the flattening of the valence bands throughout the Brillouin zone, it does not and cannot reproduce other large-scale changes to the spectral function including the increased band separation at Γ.

To visualize the degree of the electron localization in a way that permits comparison, we plot the effective masses as a function of the superlattice vector for both the upper and lower bands (Fig. 4, A and B). In each case, the effective masses m^* are directly extracted from the dispersion relations in Fig. 3 (A and B), by curve-fitting for the peak locations $E(k)$ at fixed k and fitting the resultant peaks for the local band curvature using a parabolic band approximation

$$E(k) = \frac{\hbar^2 k^2}{2m^*}$$

We find that the upper and lower valence bands are strongly renormalized in WS_2/WSe_2 heterostructures with large moiré wave

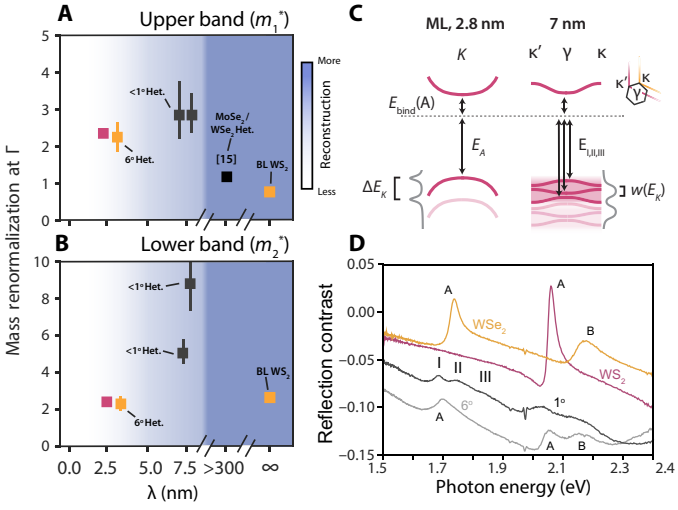

Fig. 4. Evolution of localization and excitons in heterostructures. (**A** and **B**) Renormalized mass in a variety of related bilayers, arranged by lattice constant from short wave vector through very-long-wavelength superlattices. As strong coupling is reached at moderate values of λ, the renormalized mass increases and electrons are localized at the band extrema. Moving further, reconstruction into commensurate domains is possible and the effective mass again becomes small. The case of the homobilayer is taken as an archetypal superlattice with $\lambda = \infty$ or, alternatively, the limit that $\theta \to 0$. (**C**) The exciton binding energy, optical gap, and electronic gap are related to one another through energy conservation. In moiré superlattices, mini-band formation due to zone folding allows additional peaks in the reflection contrast signal because transitions to the mini-bands have finite oscillator strength. Despite resolution limits precluding direct measurements of the mini-band structure, mini-band formation increases the apparent linewidth $w(E_k)$ by an amount comparable to the exciton peak splitting (≈150 meV) in (C). (**D**) Reflection contrast spectroscopy for each of the samples. Moiré exciton peaks are observed only for samples with angle less than about 1° (dark gray, corresponding to Fig. 2D).

vectors. The valence band (corresponding to m_1^* in Fig. 3, A and B) is more weakly renormalized than the next lowest energy band. In the latter case, masses are lower bounded by $\approx 5m_0$ and $\approx 8m_0$ in two different λ = 7 nm samples (see the Supplementary Materials), while for the valence band, the value is close to $3m_0$. The renormalization for λ = 7 nm samples may also include contributions due to multilayer splitting as well as those due to moiré effects: A moderate increase in the lower band mass is observed in TMDC bilayers and multilayers. Together with the increased separation between the bands at Γ, this asymmetry between the upper and lower bands demonstrates a substantial role for interlayer hybridization in dictating the band structure of moirés. In the case of λ = 7 nm samples, the masses presented place practical lower but not upper bounds on the degree of valence band localization because a large enough momentum range (>0.25 Å^{-1}) to observe band dispersion is required to form a mass estimate—momentum ranges smaller than ≈0.2 Å^{-1}, which are frequently used in assessing the effective mass of TMDCs in ARPES, are consistent with completely flat valence band edges.

DISCUSSION

Although it is not possible to construct superlattices with λ > 8 nm in WS_2/WSe_2 due to the 4.4% lattice incommensuration, it is useful to treat $MX_2/M'X'_2$ superlattices in a uniform way by examining the relationship between λ across chemical families and in using the effective mass as a correlate of localization. In the limit of very large λ, the superlattice is allowed to reconstruct into commensurate or nearly commensurate domains of constant local stacking separated by narrow domain walls (*28*, *29*). In this case, the mass measured by ARPES should be expected to return to the unrenormalized value. This return occurs because ARPES measures the spectral function averaged over different types of domains and the 2D commensurate stacking regions dominate 1D domain walls in area as λ grows. This relationship between the effective mass, a measure of localization that is spatially averaged over states contributing to intensity near a given band, and the structure of the superlattice potential is explored in terms of our superlattice tight-binding model in the Supplementary Materials.

Enough examples are available in the literature on other heterostructure systems [notably, $MoSe_2/WSe_2$ (*15*)] that WS_2/WSe_2, which represents the unique middle ground where superlattice effects are robust and the nearly high symmetry regions in the superlattice are highly localized, can be put in this context. For this purpose, we also adopt native homobilayers as analogs to twisted homobilayers as $\lambda \to \infty$, $\theta \to 0$. The results are plotted together with our experimental values in Fig. 4 (A and B). In reported systems where the superlattice wavelength becomes very long as is possible in twisted homobilayers and in $MoSe_2/WSe_2$, nearly the entire superlattice is reconstructed (darker shaded region, Fig. 4, A and B) into extended regions of well-defined stacking order. In this limit, the measured mass is small. The very large λ situation stands in clear contrast to the regime $(1 \ll \frac{\lambda}{\text{nm}} \ll 100)$ occupied by WS_2/WSe_2, where well-defined stacking orders make up only a small portion of the superlattice and the low-energy states are very localized. By contextualizing WS_2/WSe_2 among other TMDC heterostructures measured by ARPES, we can see that the $(1 \ll \frac{\lambda}{\text{nm}} \ll 100)$ regime occupied by aligned WS_2/WSe_2 is unique among measured candidate materials in maximizing electron localization.

A final consideration is how the electronic and optical properties evolve together in the moiré regime. Flattening and an increase in the linewidth, reported in Fig. 3E, of bands in the λ = 7.0 nm sample are consistent with the emergence of superlattice mini-bands at the *K*-point band edge. Neglecting complications introduced by superlattice selection rules (*30*) and variations in the exciton binding energy, which should be smaller than variations in the local electronic gap (*10*, *31*), mini-band formation provides a consistency between optical and ARPES results. Electronic mini-band formation, or equivalently superlattice periodic variation in the electronic gap, drives a superlattice varying optical bandgap, which results in a splitting of the exciton binding energies into sequences of peaks—moiré excitons (*9*–*11*). This picture is shown schematically in Fig. 4C for each of the λ = 2.8 nm and λ = 7.0 nm cases.

By performing absorption contrast spectroscopy measurements on the same samples we used for ARPES (Fig. 4D), we observed that the splitting of the exciton lines, attributed to the moiré, exactly accompanies the valence band flattening we observe in ARPES in each of our aligned samples, linking these phenomena as part of a consistent complex of superlattice phenomenology. Because of their very small size, direct observation of these *K*-point mini-bands by current ARPES experiments is difficult. One observable consequence, however, is that the unfolded mini-bands will increase the linewidth of the band at the *K* point and as shoulders in the EDC at *K*. This effect is annotated in Fig. 4C as an increase in $w(E_k)$. Our results directly demonstrate this widening and show a series of peak shoulders

consistent with mini-band formation at *K* (Supplementary Materials). Because ARPES on undoped samples cannot resolve the single particle gap, the linewidth increase at the *K* point in ARPES only provides half of the picture. Nonetheless, the order of magnitude correspondence between these phenomena is consistent with an origin for the moiré exciton peak structure, which comes from supercell periodic modulations in the single particle gap. Phenomenological agreement between ARPES and reflectance contrast spectroscopy firmly places our ARPES results in the broader context of TMDC moiré physics.

The same linewidth broadening effect at *K*, because of the presence of mini-bands, or equivalently different low-energy stacking configurations in the unit cell, presents as an increase in the linewidth also at Γ. The net effect across the Brillouin zone is that mini-band formation decreases the apparent resolution of photoemission measurements on moiré WS_2/WSe_2. The relationship between intrinsic effects, sample quality, and resolution is explored in more depth in the Supplementary Materials.

Together, our results put strong constraints on the theory of moiré superlattices and indicate that interlayer hybridization plays a notable role in the strongly coupled regime. The energy scale ΔE_1 at the Γ point is much larger than the energy scales for mini-band separation proposed at *K* but are closer to the values observed for the valence band separation in homobilayers where it is the interlayer interaction that is relevant. This experimental evidence indicates that the extremely large renormalization effects observed at Γ are due to the orbital composition. Whereas the orbital texture at the *K* point in the valence band is composed of largely in-plane *d* and *p* orbitals, out-of-plane d_{3z2-r2} and p_z orbitals predominate at Γ (*32*, *33*). This orbital texture and interlayer hybridization is responsible for splitting of the bands at Γ into a nondegenerate set of states in bilayer and multilayer MX_2 (*33*). In regions of the supercell resembling high-symmetry stacking, orbital hybridization should lead to appreciable bilayer splitting as we observe in our ARPES data. Because this hybridization depends on the local stacking registry, it is reasonable to presume a role for inhomogeneous hybridization in flattening the Γ point bands, as we observe, in addition to creating the bilayer-like splitting. The inevitable conclusion is that the phenomenology in moiré superlattices is much richer than currently appreciated by experiments that access primarily the lowest energy states: Hybridization, strain, and coexisting superlattice orders (section S8) may all be comparably relevant to engineering electronic behavior in a moiré.

In summary, using combined optical absorption spectroscopy and ARPES, we report the first direct, momentum-resolved measurements of the electronic properties of WS_2/WSe_2 superlattices across both the weakly and strongly modified regimes. Our measurements indicate marked differences between the spectral functions of heterostructures with increasing superlattice wavelength and the existence of qualitatively different regimes. Near the largest supercell achievable via WS_2/WSe_2 lattice engineering, we observe a large increase in the renormalized electron mass—corresponding to a quantifiable spatial localization in the superlattice—at the band edges, the formation of a gap at high energy along the dispersing valence band, and a large splitting in energy between the lowest energy states at Γ. Further, our results are the first momentum-direct measurements of moiré band reconstruction in TMDC heterostructures and demonstrate a consistent electronic and optical phenomenology. Our results point to the importance of interlayer physics and hybridization in setting the low-energy band structure and as potential key ingredients to drive the emergence of correlated phases in superlattices. Unraveling the relationship between localization and hybridization effects—whether these are independent and if they can be controlled independently—should be an essential next step toward truly engineering correlations in TMDC moirés.

MATERIALS AND METHODS

Sample preparation

The full fabrication details are available in the Supplementary Materials. Briefly, monolayers of each of WS_2 and WSe_2 and multilayered flakes of graphite and hBN were exfoliated onto Si chips with 285-nm SiO_2 with scotch tape and identified by optical microscopy. Samples composed of monolayer WS_2 or WSe_2 and graphite were assembled either at small angle or at alignment (0°, 60°) after identification of the crystal axes by second-harmonic generation. We used a dry transfer procedure either using a PPC-based stamp inversion followed by vacuum annealing (*23*) or by a sequential pickup and release with polyethylene terephthalate stamp (*34*). The completed van der Waals heterostructure composed of the WS_2/WSe_2 heterobilayer and the substate of graphite or thin (≤20 nm) hBN flake were placed on highly doped p-type silicon chips appropriate for electrically grounded photoemission experiments.

Optical spectroscopy and atomic force microscopy

The samples were loaded into a vacuum cryostat and cooled to 77 K with liquid nitrogen for reflection contrast spectroscopy measurement. The spectroscopy measurement was conducted using a supercontinuum laser focused to a spot size of 2 μm. The thickness of the hBN or graphite flakes under the WS_2/WSe_2 moiré superlattice was determined using atomic force microscopy (Park NX-20) with tapping mode at ambient condition.

Photoemission measurement

After introduction to vacuum (better than 1×10^{-9} mbar), the samples were annealed at 600 K for 8 hours to remove air from the surfaces and remaining polymer residues. Samples were then transferred into the measurement chamber (better than 1×10^{-10} mbar) for nano-ARPES experiments conducted at room temperature and at 55 K. Using either a capillary optic or a Fresnel zone plate, x-rays were focused to 1.6 μm as measured in situ by edge contrast (see the Supplementary Materials). The energy resolution during the experiment was 50 meV, and the angular resolution was better than 0.1°/0.001 $Å^{-1}$. Experiments were performed at the Advanced Light Source's MAESTRO (nano- and micro-ARPES) and at the ANTARES beamline at Synchrotron SOLEIL (nano-ARPES).

SUPPLEMENTARY MATERIALS

Supplementary material for this article is available at https://science.org/doi/10.1126/sciadv.abf4387

REFERENCES AND NOTES

1. X. Lu, P. Stepanov, W. Yang, M. Xie, M. A. Aamir, I. Das, C. Urgell, K. Watanabe, T. Taniguchi, G. Zhang, A. Bachtold, A. H. MacDonald, D. K. Efetov, Superconductors, orbital magnets and correlated states in magic-angle bilayer graphene. *Nature* **574**, 653–657 (2019).
2. A. L. Sharpe, E. J. Fox, A. W. Barnard, J. Finney, K. Watanabe, T. Taniguchi, M. A. Kastner, D. Goldhaber-Gordon, Emergent ferromagnetism near three-quarters filling in twisted bilayer graphene. *Science* **365**, 605–608 (2019).

3. Y. Tang, L. Li, T. Li, Y. Xu, S. Liu, K. Barmak, K. Watanabe, T. Taniguchi, A. H. MacDonald, J. Shan, K. F. Mak, Simulation of Hubbard model physics in WSe_2/WS_2 moiré superlattices. *Nature* **579**, 353–358 (2020).
4. Y. Cao, V. Fatemi, S. Fang, K. Watanabe, T. Taniguchi, E. Kaxiras, P. Jarillo-Herrero, Unconventional superconductivity in magic-angle graphene superlattices. *Nature* **556**, 43–50 (2018).
5. L. Wang, E.-M. Shih, A. Ghiotto, L. Xian, D. A. Rhodes, C. Tan, M. Claassen, D. M. Kennes, Y. Bai, B. Kim, K. Watanabe, T. Taniguchi, X. Zhu, J. Hone, A. Rubio, A. N. Pasupathy, C. R. Dean, Correlated electronic phases in twisted bilayer transition metal 375 dichalcogenides. *Nat. Mater.* **19**, 861–866 (2020).
6. G. Chen, A. L. Sharpe, P. Gallagher, I. T. Rosen, E. J. Fox, L. Jiang, B. Lyu, H. Li, K. Watanabe, T. Taniguchi, J. Jung, Z. Shi, D. Goldhaber-Gordon, Y. Zhang, F. Wang, Signatures of tunable superconductivity in a trilayer graphene moiré superlattice. *Nature* **572**, 215–219 (2019).
7. Y. Cao, V. Fatemi, A. Demir, S. Fang, S. L. Tomarken, J. Y. Luo, J. D. Sanchez-Yamagishi, K. Watanabe, T. Taniguchi, E. Kaxiras, R. C. Ashoori, P. Jarillo-Herrero, Correlated insulator behaviour at half-filling in magic-angle graphene superlattices. *Nature* **556**, 80–84 (2018).
8. E. C. Regan, D. Wang, C. Jin, M. I. B. Utama, B. Gao, X. Wei, S. Zhao, Z. Zhang, K. Yumigeta, M. Blei, J. D. Carlström, K. Watanabe, T. Taniguchi, S. Tongay, M. Crommie, Z. Zettl, F. Wang, Mott and generalized Wigner crystal states in WSe_2/WS_2 moiré superlattices. *Nature* **579**, 359–363 (2020).
9. C. Jin, E. C. Regan, A. Yan, M. I. B. Utama, D. Wang, S. Zhao, Y. Qin, S. Yang, Z. Zheng, S. Shi, K. Watanabe, T. Taniguchi, S. Tongay, A. Zettl, F. Wang, Observation of moiré excitons in WSe_2/WS_2 heterostructure superlattices. *Nature* **567**, 76–80 (2019).
10. K. Tran, G. Moody, F. Wu, X. Lu, J. Choi, K. Kim, A. Rai, D. A. Sanchez, J. Quan, A. Singh, J. Embley, A. Zepeda, M. Campbell, T. Autry, T. Taniguchi, K. Watanabe, N. Lu, S. K. Banerjee, K. L. Silverman, S. Kim, E. Tutuc, L. Yang, A. H. MacDonald, X. Li, Evidence for moiré excitons in van der Waals heterostructures. *Nature* **567**, 71–75 (2019).
11. E. M. Alexeev, D. A. Ruiz-Tijerina, M. Danovich, M. J. Hamer, D. J. Terry, P. K. Nayak, S. Ahn, S. Pak, J. Lee, J. I. Sohn, M. R. Molas, M. Koperski, K. Watanabe, T. Taniguchi, K. S. Novoselov, R. V. Gorbachev, H. S. Shin, V. I. Fal'ko, A. I. Tartakovskii, Resonantly hybridized excitons in moiré superlattices in van der Waals heterostructures. *Nature* **567**, 81–86 (2019).
12. J. Zribi, L. Khalil, B. Zheng, J. Avila, D. Pierucci, T. Brulé, J. Chaste, E. Lhuillier, M. C. Asensio, A. Pan, A. Ouerghi, Strong interlayer hybridization in the aligned SnS_2/WSe_2 hetero-bilayer structure. *npj 2D Mater. Appl.* **3**, 27 (2019).
13. P.-C. Yeh, W. Jin, N. Zaki, J. Kunstmann, D. Chenet, G. Arefe, J. T. Sadowski, J. I. Dadap, P. Sutter, J. Hone, R. M. Osgood, Direct measurement of the tunable electronic structure of bilayer MoS_2 by interlayer twist. *Nano Lett.* **16**, 953–959 (2016).
14. S. Park, T. Schultz, A. Han, A. Aljarb, X. Xu, P. Beyer, A. Opitz, R. Ovsyannikov, L.-J. Li, M. Meissner, T. Yamaguchi, S. Kera, P. Amsalem, N. Koch, Electronic band dispersion determination in azimuthally disordered transition-metal dichalcogenide monolayers. *Commun. Phys.* **2**, 68 (2019).
15. N. R. Wilson, P. V. Nguyen, K. Seyler, P. Rivera, A. J. Marsden, Z. P. L. Laker, G. C. Constantinescu, V. Kandyba, A. Barinov, N. D. M. Hine, X. Xu, D. H. Cobden, Determination of band offsets, hybridization, and exciton binding in 2D semiconductor heterostructures. *Sci. Adv.* **3**, e1601832 (2017).
16. C. Kastl, C. T. Chen, R. J. Koch, B. Schuler, T. R. Kuykendall, A. Bostwick, C. Jozwiak, T. Seyller, E. Rotenberg, A. Weber-Bargioni, S. Aloni, A. M. Schwartzberg, Multimodal spectromicroscopy of monolayer WS_2 enabled by ultra-clean van der Waals epitaxy. *2D Mater.* **5**, 045010 (2018).
17. H. Nakamura, A. Mohammed, P. Rosenzweig, K. Matsuda, K. Nowakowski, K. Küster, P. Wochner, S. Ibrahimkutty, U. Wedig, H. Hussain, J. Rawle, C. Nicklin, B. Stuhlhofer, G. Cristiani, G. Logvenov, H. Takagi, U. Starke, Spin splitting and strain in epitaxial monolayer WSe_2 on graphene. *Phys. Rev. B.* **101**, 165103 (2020).
18. G.-B. Liu, D. Xiao, Y. Yao, X. Xu, W. Yao, Electronic structures and theoretical modelling of two-dimensional group-VIB transition metal dichalcogenides. *Chem. Soc. Rev.* **44**, 2643–2663 (2015).
19. S. Fang, R. Kuate Defo, S. N. Shirodkar, S. Lieu, G. A. Tritsaris, E. Kaxiras, Ab initio tight-binding Hamiltonian for transition metal dichalcogenides. *Phys. Rev. B* **92**, 205108 (2015).
20. Y.-C. Lin, C.-Y. S. Chang, R. K. Ghosh, J. Li, H. Zhu, R. Addou, B. Diaconescu, T. Ohta, X. Peng, N. Lu, M. J. Kim, J. T. Robinson, R. M. Wallace, T. S. Mayer, S. Datta, L.-J. Li, J. A. Robinson, Atomically thin heterostructures based on single-layer tungsten diselenide and graphene. *Nano Lett.* **14**, 6936–6941 (2014).
21. J. Gusakova, X. Wang, L. L. Shiau, A. Krivosheeva, V. Shaposhnikov, V. Borisenko, V. Gusakov, B. K. Tay, Electronic properties of bulk and monolayer TMDs: Theoretical study within DFT framework (GVJ-2e method). *Phys. Stat. Solidi (A)* **214**, 1700218 (2017).
22. L. Waldecker, A. Raja, M. Rösner, C. Steinke, A. Bostwick, R. J. Koch, C. Jozwiak, T. Taniguchi, K. Watanabe, E. Rotenberg, T. O. Wehling, T. F. Heinz, Rigid band shifts in two-dimensional semiconductors through external dielectric screening. *Phys. Rev. Lett.* **123**, 206403 (2019).
23. M. I. B. Utama, R. J. Koch, K. Lee, N. Leconte, H. Li, S. Zhao, L. Jiang, J. Zhu, K. Watanabe, T. Taniguchi, P. D. Ashby, A. Weber-Bargioni, A. Zettl, C. Jozwiak, J. Jung, E. Rotenberg, A. Bostwick, F. Wang, Visualization of the flat electronic band in twisted bilayer graphene near the magic angle twist. *Nat. Phys.* , 184–188 (2020).
24. S. Lisi, X. Lu, T. Benschop, T. A. de Jong, P. Stepanov, J. R. Duran, F. Margot, I. Cucchi, E. Cappelli, A. Hunter, A. Tamai, V. Kandyba, A. Giampietri, A. Barinov, J. Jobst, V. Stalman, M. Leeuwenhoek, K. Watanabe, T. Taniguchi, L. Rademaker, S. J. van der Molen, M. P. Allan, D. K. Efetov, F. Baumberger, Observation of flat bands in twisted bilayer graphene. *Nat. Phys.* **17**, 189–193 (2021).
25. S. Appelfeller, K. Holtgrewe, M. Franz, L. Freter, C. Hassenstein, H.-F. Jirschik, S. Sanna, M. Dähne, Continuous crossover from two-dimensional to one-dimensional electronic properties for metallic silicide nanowires. *Phys. Rev. B* **102**, 115433 (2020).
26. P. Puschnig, D. Lüftner, Simulation of angle-resolved photoemission spectra by approximating the final state by a plane wave: From graphene to polycyclic aromatic hydrocarbon molecules. *J. Electron Spectros. Relat. Phenom.* **200**, 193–208 (2015).
27. H. Li, S. Li, M. H. Naik, J. Xie, X. Li, J. Wang, E. Regan, D. Wang, W. Zhao, S. Zhao, S. Kahn, K. Yumigeta, M. Blei, T. Taniguchi, K. Watanabe, S. Tongay, A. Zettl, S. G. Louie, F. Wang, M. F. Crommie, Imaging moiré flat bands in three-dimensional reconstructed WSe_2/WS_2 superlattices. *Nat. Mater.* **20**, 945–950 (2021).
28. A. Weston, Y. Zou, V. Enaldiev, A. Summerfield, N. Clark, V. Zólyomi, A. Graham, C. Yelgel, S. Magorrian, M. Zhou, J. Zultak, D. Hopkinson, A. Barinov, T. H. Bointon, A. Kretinin, N. R. Wilson, P. H. Beton, V. I. Fal'ko, S. J. Haigh, R. Gorbachev, Atomic reconstruction in twisted bilayers of transition metal dichalcogenides. *Nat. Nanotechnol.* **15**, 592–597 (2020).
29. M. H. Naik, M. Jain, Ultraflatbands and shear solitons in moiré patterns of twisted bilayer transition metal dichalcogenides. *Phys. Rev. Lett.* **121**, 266401 (2018).
30. C. Jin, E. C. Regan, D. Wang, M. I. B. Utama, C.-S. Yang, J. Cain, Y. Qin, Y. Shen, Z. Zheng, K. Watanabe, T. Taniguchi, S. Tongay, A. Zettl, F. Wang, Identification of spin, valley and moiré quasi-angular momentum of interlayer excitons. *Nat. Phys.* **15**, 1140–1144 (2019).
31. F. Wu, T. Lovorn, A. H. MacDonald, Topological exciton bands in moiré heterojunctions. *Phys. Rev. Lett.* **118**, 147401 (2017).
32. J. Á. Silva-Guillén, P. San-Jose, R. Roldán, Electronic band structure of transition metal dichalcogenides from ab initio and Slater–Koster tight-binding model. *Appl. Sci.* **6**, 284 (2016).
33. M. H. Naik, M. Jain, Origin of layer dependence in band structures of two-dimensional materials. *Phys. Rev. B* **95**, 165125 (2017).
34. C. Jin, J. Kim, M. I. B. Utama, E. C. Regan, H. Kleemann, H. Cai, Y. Shen, M. J. Shinner, A. Sengupta, K. Watanabe, T. Taniguchi, S. Tongay, A. Zettl, F. Wang, Imaging of pure spin-valley diffusion current in WS_2-WSe_2 heterostructures. *Science* **360**, 893–896 (2018).
35. C. Stansbury, A. Lanzara, PyARPES: An analysis framework for multimodal angle-resolved photoemission spectroscopies. *SoftwareX* **11**, 100472 (2020).
36. D. Moldovan, M. Anđelković, F. Peeters, pybinding v0.9.4: A Python package for tight-binding calculations. Zenodo (2017); https://zenodo.org/record/826942.
37. Y. Li, Y. Rao, K. F. Mak, Y. You, S. Wang, C. R. Dean, T. F. Heinz, Probing symmetry properties of few-layer MoS_2 and h-BN by optical second-harmonic generation. *Nano Lett.* **13**, 3329–3333 (2013).
38. C. Zhang, C.-P. Chuu, X. Ren, M.-Y. Li, L.-J. Li, C. Jin, M.-Y. Chou, C.-K. Shih, Interlayer couplings, Moiré patterns, and 2D electronic superlattices in MoS_2/WSe_2 hetero-bilayers. *Sci. Adv.* **3**, e1601459 (2017).
39. S. Brem, C. Linderälv, P. Erhart, E. Malic, Tunable phases of Moiré excitons in van der Waals heterostructures. *Nano Lett.* **20**, 8534–8540 (2020).
40. G.-B. Liu, W.-Y. Shan, Y. Yao, W. Yao, D. Xiao, Three-band tight-binding model for monolayers of group-VIB transition metal dichalcogenides. *Phys. Rev. B* **88**, 085433 (2013).
41. H. Nishi, Y. Matsushita, A. Oshiyama, Band-unfolding approach to moiré-induced band-gap opening and Fermi level velocity reduction in twisted bilayer graphene. *Phys. Rev. B* **95**, 085420 (2017).

Acknowledgments: We thank D.-H. Lee and E. Thewalt for useful discussions. We acknowledge S. Kahn for technical assistance. ARPES data analysis was conducted with the PyARPES software package (*35*), and the supercell tight-binding models were constructed with the aid of pybinding (*36*). **Funding:** Both the experimental and theoretical parts of this work were primarily supported as part of the Center for Novel Pathways to Quantum Coherence in Materials, an Energy Frontier Research Center funded by the U.S. Department of Energy, Office of Science, Basic Energy Sciences. C.H.S. and A.L. also acknowledge the Director, Office of Science, Office of Basic Energy Sciences, Materials Sciences and Engineering Division, of the U.S. Department of Energy, under contract no. DE-AC02-05CH11231, as part of the Ultrafast Materials Science Program (KC2203) which has supported the development of analysis

software used in this paper.. C.G.F. acknowledges support from the Swiss National Science Foundation through the fellowship P2ELP_175282. K.W. and T.T. acknowledge support from the Elemental Strategy Initiative, conducted by the MEXT, Japan, grant number JPMXP0112101001, and JSPS KAKENHI grant numbers JP20H00354 and CREST (JPMJCR15F3), JST. E.C.R. acknowledges support from the Department of Defense (DoD) through the National Defense Science and Engineering Graduate Fellowship (NDSEG) Program. S.T. acknowledges support from DOE-SC0020653, NSF DMR 1552220, DMR 1904716, and NSF CMMI 1933214.
Author contributions: The project was initiated and overseen by C.H.S., M.I.B.U., F.W., and A.L. C.H.S., C.G.F., and M.I.B.U. performed ARPES measurements. M.I.B.U. carried out optical measurements. C.H.S. performed data and theoretical analysis and the tight-binding calculations. M.I.B.U., C.H.S., M.D., Z.X., E.C.R., and D.W. fabricated van der Waals heterostructures. R.K., A.B., C.J., S.L., J.A., and E.R. developed nano-ARPES instrumentation and assisted with ARPES measurements. Y.S., M.B., and S.T. grew WS_2 and WSe_2 crystals. K.W. and T.T. grew hexagonal boron nitride crystals. C.H.S., M.I.B.U., and A.L. wrote the manuscript.

Competing interests: The authors declare that they have no competing interests. **Data and materials availability:** All data needed to evaluate the conclusions in the paper are present in the paper and/or the Supplementary Materials.

Submitted 28 October 2020
Accepted 21 July 2021
Published 10 September 2021
10.1126/sciadv.abf4387

Citation: C. H. Stansbury, M. I. B. Utama, C. G. Fatuzzo, E. C. Regan, D. Wang, Z. Xiang, M. Ding, K. Watanabe, T. Taniguchi, M. Blei, Y. Shen, S. Lorcy, A. Bostwick, C. Jozwiak, R. Koch, S. Tongay, J. Avila, E. Rotenberg, F. Wang, A. Lanzara, Visualizing electron localization of WS_2/WSe_2 moiré superlattices in momentum space. *Sci. Adv.* **7**, eabf4387 (2021).